

**Resolution of strongly competitive product channels with optimal dynamic discrimination: Application to flavins**

Jonathan Roslund, Matthias Roth, Laurent Guyon, Véronique Boutou, Francois Courvoisier, Jean-Pierre Wolf, and Herschel Rabitz

Citation: [The Journal of Chemical Physics](#) **134**, 034511 (2011); doi: 10.1063/1.3518751

View online: <http://dx.doi.org/10.1063/1.3518751>

View Table of Contents: <http://scitation.aip.org/content/aip/journal/jcp/134/3?ver=pdfcov>

Published by the [AIP Publishing](#)

---



## Re-register for Table of Content Alerts

Create a profile.



Sign up today!



# Resolution of strongly competitive product channels with optimal dynamic discrimination: Application to flavins

Jonathan Roslund,<sup>1,a)</sup> Matthias Roth,<sup>1</sup> Laurent Guyon,<sup>2</sup> Véronique Boutou,<sup>2</sup> Francois Courvoisier,<sup>2,3</sup> Jean-Pierre Wolf,<sup>3</sup> and Herschel Rabitz<sup>1</sup>

<sup>1</sup>Department of Chemistry, Princeton University, Princeton, New Jersey 08544, USA

<sup>2</sup>Université Lyon 1, LASIM, UMR CNRS 5579, 43 bd du 11 Novembre 1918, F69622 Villeurbanne Cedex, France

<sup>3</sup>GAP, University of Geneva, 20 rue de l'Ecole de Medecine, CH 1211 Geneva 4, Switzerland

(Received 25 May 2010; accepted 2 November 2010; published online 21 January 2011)

Fundamental molecular selectivity limits are probed by exploiting laser-controlled quantum interferences for the creation of distinct spectral signatures in two flavin molecules, erstwhile nearly indistinguishable via steady-state methods. Optimal dynamic discrimination (ODD) uses optimally shaped laser fields to transiently amplify minute molecular variations that would otherwise go unnoticed with linear absorption and fluorescence techniques. ODD is experimentally demonstrated by combining an optimally shaped UV pump pulse with a time-delayed, fluorescence-depleting IR pulse for discrimination amongst riboflavin and flavin mononucleotide in aqueous solution, which are structurally and spectroscopically very similar. Closed-loop, adaptive pulse shaping discovers a set of UV pulses that induce disparate responses from the two flavins and allows for concomitant flavin discrimination of  $\sim 16\sigma$ . Additionally, attainment of ODD permits quantitative, analytical detection of the individual constituents in a flavin mixture. The successful implementation of ODD on quantum systems of such high complexity bodes well for the future development of the field and the use of ODD techniques in a variety of demanding practical applications. © 2011 American Institute of Physics. [doi:10.1063/1.3518751]

## I. INTRODUCTION

The identification and discrimination of target molecules in the presence of structurally and spectroscopically similar background agents is a challenge that abounds in multiple areas of science and engineering. In this regard, various circumstances arise where molecular systems of interest exhibit diffuse, overlapping, or unstructured spectra, thus inhibiting their unambiguous recognition and detection with conventional optical spectroscopic techniques. Such a problem is exemplified by live tissue assays with linear fluorescence spectroscopy; in this case, fluorescence is typically emitted by various sources, including amino acids (tryptophan) and metabolic cofactors (NADH and flavins), and the combined featureless, overlapping spectra render identification of individual compounds nearly impossible. In such a situation, meaningful discrimination amongst fluorophores must overcome similarities of the optical spectra induced by environmental inhomogeneities, solvent-induced line broadening, etc.

Notwithstanding the above circumstances, two systems that appear essentially indistinguishable by static spectroscopic means may respond quite uniquely to an optimally shaped ultrafast optical field. Hence, the lack of readily identifiable information from linear spectra may be overcome through careful observation and control of the nonlinear responses displayed by similar molecular species. As

a preliminary demonstration of this concept, unshaped femtosecond pulses have been effective at exploiting ultrafast dynamics to differentiate aerosolized bacteria from other atmospheric particles.<sup>1</sup> While bioaerosols such as tryptophan and riboflavin (RBF) share similar linear, static spectra with traffic-related urban hydrocarbon aerosols, the action of an ultrafast pump pulse and suitably time-delayed probe reveals distinct temporal responses that permit reliable discrimination.<sup>2,3</sup> Variation of the time-delay between the two pulses serves as a form of one-dimensional pulse shaping and is able to induce distinct temporal responses between the hydrocarbons and biological compounds. Nevertheless, a simple pump-probe scheme is unable to induce sufficiently disparate nonlinear responses amongst various flavins; in the present circumstance, nonlinear refers to the coordinated action of both the pump and probe pulses. Alternatively, flexible optical pulse shaping may be employed to craft a custom nonlinear response for exceedingly similar biological fluorophores.

The above concept exemplifies the broad utility of optimally shaped femtosecond laser fields to coherently alter quantum dynamics, which is receiving much attention<sup>4,5</sup> and has successfully been applied to an array of chemical,<sup>6–8</sup> physical,<sup>9,10</sup> and biological systems.<sup>11,12</sup> This experimental realization has been enabled by a confluence of ultrafast laser pulse shaping capabilities,<sup>13</sup> high repetition rate femtosecond sources,<sup>14</sup> and efficient, high-dimensional evolutionary algorithms.<sup>15</sup> Yet, the vast majority of examined systems have relied on accessible product channels well separated in state space (e.g., targeted electronic state excitation in the presence of other competing states). Whereas selective excitation

<sup>a)</sup> Author to whom correspondence should be addressed. Electronic mail: jroslund@princeton.edu.

has been examined,<sup>16–18</sup> the practical capacity for high fidelity control amongst poorly resolved channels is largely unknown and unexplored. Recent theoretical evidence indicates that realistic quantum systems differing even infinitesimally may be practically differentiated by means of their dynamic evolution when acted upon with an optimally shaped pulse.<sup>19,20</sup> Such optimal dynamic discrimination (ODD) provides a means to transiently resolve the product channels of quantum systems with nearly indistinguishable initial states. The present work builds upon the one-parameter control of pump–repump schemes<sup>1–3</sup> and utilizes the full flexibility of adaptive, feedback pulse shaping to accomplish discrimination amongst cellular agents exhibiting nearly identical linear spectra.

A precursory report examining the efficacy of ODD for discrimination amongst such competitive product channels has recently been published.<sup>21</sup> This paper expands upon that groundwork and is organized as follows. Section II provides an underpinning of the ODD concept before introducing the flavin model systems in Sec. III. The experimental setup utilized for implementation of ODD is outlined in Sec. IV. Subsequently, the learning control results and demonstration of achievable flavin selectivity are presented in Sec. V. Finally, concluding remarks and an outlook toward future development and potential applications are discussed in Sec. VI.

## II. THE OPTIMAL DYNAMIC DISCRIMINATION CONCEPT

In contrast to traditional spectroscopic techniques, ODD seeks to differentiate two statically similar quantum systems by means of their dynamics when acted upon by a suitably shaped control field  $\epsilon_c(t)$ . Subtle differences in field-free molecular Hamiltonians and transition dipoles are actively exploited and amplified so as to achieve a transient separation of initially nearly indistinguishable systems. Such dynamical control can in principle achieve dramatic levels of discrimination and provide a degree of molecular selectivity not offered by standard approaches. A heuristic outline of the ODD concept is presented below.

Each molecular species  $\nu$  in a sample mixture possesses a number  $N$  of accessible rovibronic states, ( $|\phi_1^\nu\rangle, \dots, |\phi_N^\nu\rangle$ ) in addition to a detection state  $|D^\nu\rangle$ , which corresponds to a user-specified physical observable.<sup>19</sup> Although the state vectors for all species in the sample are initially nearly parallel (i.e., statically indistinguishable), an optimally shaped control field  $\epsilon_c(t)$  interacts with the sample to create a dynamically evolving wavepacket for each system given by

$$|\psi^\nu(t)\rangle = \sum_{i=1}^N c_i^\nu(t)|\phi_i^\nu\rangle + d^\nu(t)|D^\nu\rangle, \quad \nu = 1, 2, 3, \dots, \quad (1)$$

where  $c_i^\nu(t)$  and  $d^\nu(t)$  are Schrödinger picture expansion coefficients of the rovibronic and detection states, respectively (a similar analysis utilizing the density matrix may be equivalently formulated<sup>22</sup>). Measurement of each species' detection state  $|D^\nu\rangle$  on a coherent time scale yields the final population

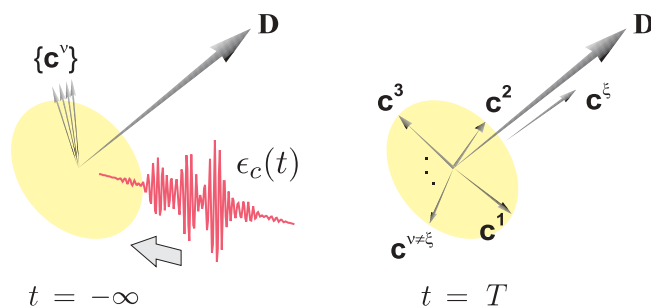


FIG. 1. ODD seeks to dynamically discriminate a number of statically similar quantum systems. The state vectors  $\mathbf{c}^\nu$  for quantum systems  $\nu = 1, 2, \dots$  are initially nearly parallel, which reflects their static indistinguishability. An optimal control pulse creates dynamic evolution of the state vectors to align the targeted quantum system  $\mathbf{c}^\xi$  parallel to the detection state  $\mathbf{D}$  and all other background systems ( $\nu \neq \xi$ ) orthogonal to the detection state. Such discrimination is achieved on a coherent time scale, after which all state vectors again resume their free evolution.

given by  $|\langle D^\nu | \psi^\nu(T) \rangle|^2 = |d^\nu(T)|^2$  and serves as feedback for optimizing the control field  $\epsilon_c(t)$ .

In practice, the unique dynamical evolution of each quantum system may be probed by any number of spectroscopies (e.g., fluorescence, absorption, mass, and Raman spectroscopies) with the constraint that the interrogation be performed on a coherent time scale. In the present incarnation of ODD, the dynamic evolution of each system is initiated with a shaped UV control pulse, and interrogation of the detection state is accomplished with a time-delayed, unshaped near-IR pulse.

Molecular specificity is maximally enhanced when only the state vector of species  $\xi$  lies parallel to the observed detection state (i.e.,  $|d^\nu(T)|^2 = 0, \nu \neq \xi$ ) as in Fig. 1. While this represents an upper theoretical limit for ODD, real experimental systems are quite complex, and experimental constraints (e.g., finite laser bandwidth, fluence, wavelength tunability, and pulse shaper resolution) practically limit the degree of attainable control. Thus, while the overall objective of ODD is enhancement of molecular specificity amongst similar quantum systems, this task need not necessarily be accomplished just by maximization of an absolute signal  $|d^\nu(T)|^2$  for a given target species. In practice, maximal discrimination amongst systems may be achieved in a variety of ways. As such, the explicit fitness function optimized by an evolutionary algorithm can assume multiple forms depending upon the specific discrimination goal, and ancillary goals may also be explicitly included in the fitness function,<sup>23</sup> such as removal of unnecessary field structure,<sup>24</sup> improving the signal-to-noise ratio,<sup>25</sup> etc.

It is also important to note that detailed knowledge of the systems under active control is not required for implementation of ODD. Although obfuscated in the steady-state spectra, the examined systems will generally contain a number of subtle, secondary structural variations; ODD seeks to discover a suitable pulse that targets and transiently amplifies such compositional differences to create a discernable dynamic signature.

Achieving such molecular specificity with realistic systems may appear unduly complex considering a host of issues, including the exceptionally high density of vibrational

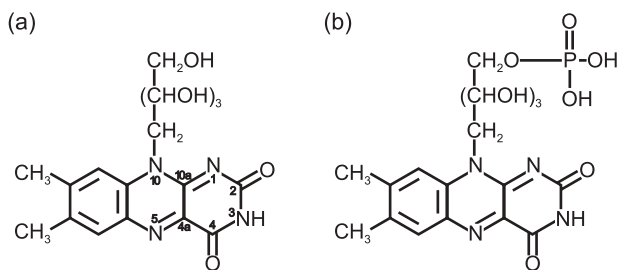


FIG. 2. Molecular structure of RBF (a) and FMN (b) with numbering of specific atoms in the isoalloxazine ring moiety.

states for even moderately sized molecules, control in a polarizable solvent, thermal population of low-frequency vibrations, and finite control resources. Nevertheless, these apparent obstacles do not necessarily preclude significant discrimination, and control studies on biological molecules<sup>11</sup> suggest that system complexity is not necessarily a hindrance. Indeed, a large density of states actually may aid the discrimination process by enabling richer controlled quantum interferences through multiple dynamical pathways. Hence, such system complexities may mitigate certain experimental constraints and enhance discrimination possibilities.

### III. RIBOFLAVIN AND FLAVIN MONONUCLEOTIDE MODEL SYSTEMS

The quantum systems explored in the present study consist of two biologically important molecules, RBF and flavin mononucleotide (FMN), whose photophysical properties have been extensively studied<sup>26</sup> due to their significant contribution to the fluorescence originating from live tissue and prominent role in cellular respiration. The common structural feature for both flavins is the central isoalloxazine ring. In the case of FMN, however, the ribityl side chain at the N<sub>10</sub> ring position is a phosphorylated version of that present in RBF (Fig. 2). This distinguishing structural feature of phosphorylation is critical for biological activation of many proteins. In this circumstance, phosphorylation of RBF to FMN is an important process for cellular metabolism as oxidation of NADH by FMN-activated NADH dehydrogenase (complex I) is the initial step of the electron transport chain. Although this slight chemical variation on the terminal side chain results in markedly distinct biological activities for RBF and FMN, the common isoalloxazine chromophore yields nearly indistinguishable photophysics, including in the electronic absorption and emission spectra (Fig. 3).

The electronic absorption spectra for both RBF and FMN (Fig. 3) consists of four strong, structureless  $\pi \rightarrow \pi^*$  type transitions with little observable contribution from  $n \rightarrow \pi^*$  transitions.<sup>26</sup> Although not plainly visible in the liquid-phase spectra, the  $0 \rightarrow 0$ ,  $0 \rightarrow 1$ , and  $0 \rightarrow 2$  vibrational progression of the  $S_0 \rightarrow S_1$  transition (indicated in Fig. 4) have been observed with a  $\sim 1200 \text{ cm}^{-1}$  spacing through low-temperature studies,<sup>27</sup> aqueous-phase CARS spectroscopy,<sup>28</sup> and in flavoproteins, where a reduction of inhomogeneous broadening is observed for the flavin chromophore fixed in a protein binding pocket.<sup>29</sup> Specifically, Franck–Condon factors shift the  $S_0 \rightarrow S_1$  absorption maximum to the  $0 \rightarrow 1$  vi-

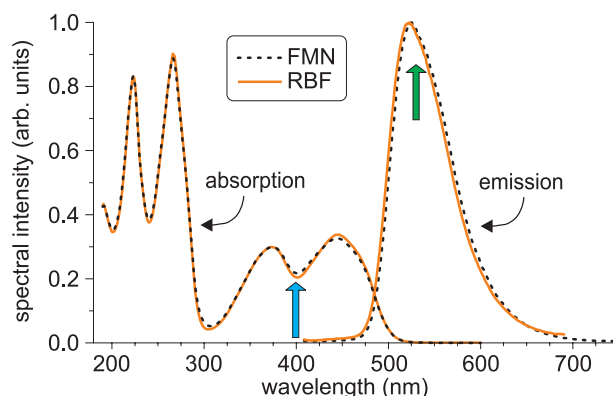


FIG. 3. Linear absorption and fluorescence spectra of RBF (solid) and FMN (dashed) in aqueous media at 298 K. Arrows at 400 and 530 nm indicate the control and collected fluorescence wavelengths, respectively.

bronic band, while the  $0 \rightarrow 0$  vibrational band is visible as a shoulder at  $\sim 475 \text{ nm}$ . Additionally, a second absorption maximum centered at 375 nm corresponds to the  $S_0 \rightarrow S_2$  electronic transition and is also significantly broadened by vibrational contributions. Hence, any spectroscopic signature of vibrational structure unique to either RBF or FMN is lost and obscured by line-broadening inhomogeneities. The energy level structure for the flavin compounds is shown in Fig. 4 along with their absorption and fluorescence spectra.

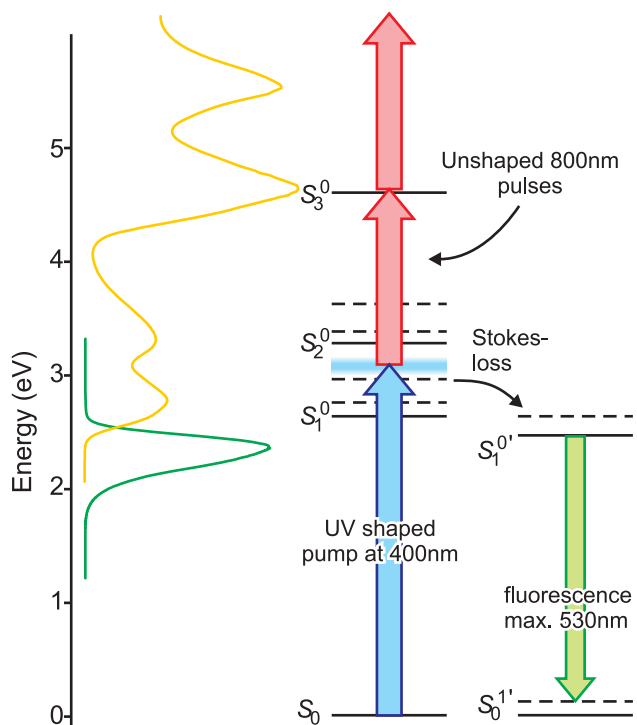


FIG. 4. Energy level diagram illustrating ODD-relevant electronic transitions for RBF and FMN; the corresponding absorption and fluorescence spectra are shown on the left. The 400 nm shaped UV control field creates a unique wavepacket in a vibrational band  $\{v\}$  of electronic state  $S_1$ . A time-delayed, unshaped IR pulse at 800 nm interrupts the carefully created wavepackets on  $S_1$  and re-excites the population to higher states  $S_2$ , thus depleting the  $S_1$  population and eventual fluorescence at 530 nm. The coherent interplay between the shaped preparation pulse, wavepacket evolution, and delayed depletion pulse induces a detectable difference in the RBF and FMN depletion efficiencies.

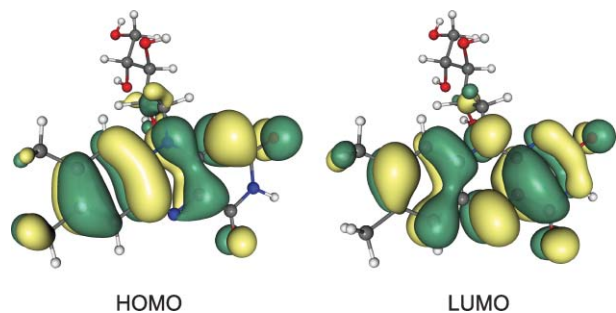


FIG. 5. Highest occupied (HOMO) and lowest unoccupied (LUMO) molecular orbitals involved in the initial  $\pi \rightarrow \pi^*$  type  $S_0 \rightarrow S_1$  electronic transition of RBF. Localization of electron density on the central isoalloxazine ring is consistent with the minor influence of the ribityl side chain on the observed photophysics. Electronic structure obtained with GAUSSIAN 03 at the B3LYP/DGTZVP level of theory.

Transition to the first excited flavin electronic state  $S_0 \rightarrow S_1$  gives rise to no change of dipole moment (i.e., no charge-transfer character) as deduced from both Stark-effect spectroscopy<sup>30</sup> and a lack of solvatochromism.<sup>31</sup> Upon populating  $S_1$ , a rearrangement of the solvent molecules ensues on a picosecond time scale and redshifts the fluorescence spectra<sup>26</sup> compared to flavins bound in a protein matrix or as would be expected for gas phase spectroscopy of flavins, which has yet to be experimentally observed. The subsequent fluorescence is centered at 520–530 nm (Fig. 3) and is emitted within a lifetime of  $\sim 5$  ns.<sup>32</sup> The fluorescence quantum yield for RBF, FMN, and lumiflavin is  $\phi_f \simeq 0.26$  and is independent of excitation wavelength, which indicates rapid conversion to low vibrational states of  $S_1$ .<sup>32,33</sup> The quantum yield depends on a variety of competing factors, such as nonradiative decay or intersystem crossing, and may be considerably altered by changes in solution pH, hydrogen bonding between the flavin and solvent molecules, or the presence of quenching molecules. Such considerations can all have an influence on the induced molecular dynamics and consequently the effectiveness of ODD.

Density functional theory calculations of the flavins indicate that the molecular orbitals involved in the  $S_0 \rightarrow S_1$  electronic transition are predominantly localized on the central isoalloxazine moiety (Fig. 5) with insignificant concentration on the  $N_{10}$  ribityl side chain, and an equivalent confinement is also observed for lumiflavin<sup>34</sup> and other flavin-related isoalloxazines.<sup>35</sup> This concentration of electron density on the central ring is consistent with the fact that the vibrational modes of the ribityl side chain exert an imperceptible influence on the flavin electronic spectral features. Interestingly, because of this negligible impact, many spectroscopic and computational studies wholly disregard the side chain variations and consider RBF, FMN, FAD, and lumiflavin as spectrally equivalent. Yet, it is precisely these minor variations in the vibronic spectra that are transiently amplified and exploited by ODD for discrimination of the flavin species.

Toward this end, it has been observed that the specific form of the side chain at the  $N_{10}$  atom slightly perturbs the vibrational dynamics of the main isoalloxazine moiety. For instance, infrared spectroscopy of lumiflavin and RBF indicates that addition of a ribityl side chain at  $N_{10}$  influences several

isoalloxazine ring vibrational modes. Intramolecular hydrogen bonding between OH groups of the ribityl moiety and the  $C_2$  carbonyl group also affect both the carbonyl vibrational frequency<sup>36,37</sup> as well as the coupling between the  $C_2=O$  stretching vibration and the  $N_3-H$  bending mode.<sup>36</sup> Finally, the terminal side chain length and flexibility results in a near-continuum of low-frequency torsional modes<sup>38</sup> whose vibrational dynamics are likely critical for the success of ODD. Although the effect of such differences between RBF and FMN is nearly undetectable with linear absorption and emission, ODD seeks to exploit and dynamically amplify such minute features that may be obscured from conventional spectroscopic techniques.

The distinction between typical coherent control experiments and the present use of ODD lies within the specific goal of the control process. Instead of driving one quantum system into a well-defined product channel that competes with alternative outcome channels, ODD seeks to disrupt the strong correspondence amongst product channels for RBF and FMN so as to affect maximally dissimilar dynamics. Notwithstanding these distinctions, the fundamental connection between ODD and coherent control implies that success of ODD in demanding circumstances is auspicious for meeting analogous control goals in a single quantum system.

## IV. EXPERIMENTAL SETUP

### A. Experimental layout

The experimental setup for the ODD learning process and subsequent discrimination is depicted in Fig. 6. A commercial Ti:Sapphire femtosecond laser system generates amplified pulses at 1 kHz, centered at 797 nm, and with a bandwidth of 10 nm, which corresponds to pulses of  $\sim 100$  fs duration [full width at half maximum (FWHM)]. A fraction of this output (160  $\mu$ J) is split off and frequency doubled in a Keplerian telescope setup with a 300- $\mu$ m-thick type-I BBO crystal close to the focal point. The process yields pulses of 60  $\mu$ J energy, centered at 399.5 nm with a bandwidth of 3.5-nm FWHM.

The UV pulses are subsequently introduced into an acousto-optic-modulator (AOM) based pulse shaper<sup>39</sup> specifically designed for the UV regime.<sup>40</sup> The digital arbitrary waveform generator driving the AOM-pulse shaper enables control over 200 effective pixels of the acoustic wave. Sequential operation by first performing frequency upconversion and then pulse shaping is a critical feature of the current setup since it avoids convolving conversion efficiency with the controlled molecular dynamics. In this manner, phase-only shaping guarantees UV pulses of constant energy. Characterization of shaped UV pulses is performed with frequency resolved optical gating based on self-diffraction (SD-FROG)<sup>40</sup> (not shown in Fig. 6). The transform-limited output pulses have a 78 fs FWHM pulse width. The residual IR beam is passed through a variable delay line in order to compensate for the path of the UV shaper.

The shaped UV and unshaped IR pulses are then recombined and collinearly focused with a  $f = 500$  mm fused silica lens whereupon the beam is split with a pellicle beam

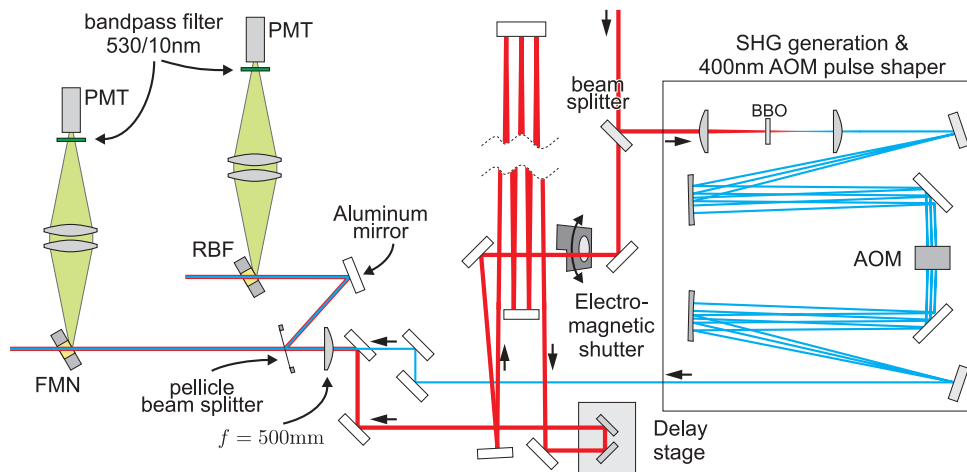


FIG. 6. Experimental layout for closed-loop ODD. The shaped UV pulse and unshaped IR pulse are recombined in duplicate flow cells each containing aqueous solutions of RBF or FMN. For the discrimination stage of the experiments, the two flow cells are replaced with a single flow cell containing an aqueous mixture of RBF and FMN. Temporally depleted fluorescence induced by the IR pulse is detected with photomultiplier modules.

splitter (Thorlabs BP145B1). The pellicle angle is adjusted so as to generate equivalent splitting ratios for both the 400 and 800 nm beams. Additionally, the pellicle thickness of  $2 \mu\text{m}$  maintains the spatial overlap conditions in both flow cells. The two beams are focused into duplicate flow cells with an optical path length of 1.5 mm and each containing  $\sim 50 \mu\text{M}$  aqueous solutions of RBF or FMN ( $\text{pH } 7.0$ ). The flow cells are positioned slightly before the focal point so as to avoid any white light generation in the  $80 \mu\text{m}$  thick windows. The energy and beam diameter for the UV pulse is  $\sim 3 \mu\text{J}$  and  $\sim 150 \mu\text{m}$ , respectively, while that of the IR interrogating pulse is  $\sim 210 \mu\text{J}$  and  $\sim 430 \mu\text{m}$ . A larger IR beam diameter significantly decreases the experimental sensitivity to any UV beam pointing instabilities. Linear absorption of the UV radiation is observed at all employed intensities; additionally, simple transition from a multiphoton to linear absorption mechanism of UV radiation with shaped pulses is also ruled out since the long-time population transfer into  $S_1$  is identical for both the transform-limited and optimal pulse (see Fig. 11).

Fluorescence from each flow cell is filtered (BG18 Schott glass) to remove scattered IR light and imaged onto distinct photomultiplier tubes (Hamamatsu H5784-01). Interference filters select the fluorescence at 530 nm with a bandwidth of 10 nm (Fig. 3). The flavin triplet state  $T_1$  primarily decays by nonradiative processes, and the reported low-yield ( $\phi_p \simeq 0.001$ ) phosphorescence at  $610 \text{ nm}$ <sup>26</sup> was not observed in the present experiments. Additionally, photofragmentation of the ribityl side chain of either flavin is not observed as evidenced by an absence of the distinct lumiflavin fluorescence spectrum.<sup>41,42</sup> All resultant fluorescence signals are recorded on a shot-to-shot basis with a boxcar integrator (SR250) and A/D converter (SR245).

## B. Temporal fluorescence depletions

The relative temporal population of the  $S_1$  state of RBF is monitored by measuring the depletion signal  $D_{\text{RBF}}(\tau) = [F_{\text{RBF}}^{\text{und}} - F_{\text{RBF}}^{\text{d}}(\tau)]/F_{\text{RBF}}^{\text{und}}$ , where  $F_{\text{RBF}}^{\text{und}}$  is the undepleted fluorescence signal from the RBF cell (i.e., in the absence of the IR pulse) and  $F_{\text{RBF}}^{\text{d}}(\tau)$  is the depleted fluorescence in the

presence of the IR pulse delayed by time  $\tau$ . An analogous expression  $D_{\text{FMN}}(\tau)$  corresponds to the separate FMN solution and is recorded with the same trial pulses. The depleted and undepleted fluorescence signals are each obtained by averaging 1000 individual laser shots, and an electromagnetic shutter (Fig. 6) serves to sequentially block and then pass the IR pulse. Depletion of the  $S_1$  fluorescence for RBF and FMN as a function of the unshaped UV–IR time-delay  $\tau$  is shown in Fig. 7. When the IR pulse precedes the UV pulse, the depletion of both compounds is zero; additionally, the IR pulse is of insufficient intensity to generate fluorescence from direct two-photon absorption. ODD experiments are performed for delays between 200 and 600 fs (gray area in Fig. 7), as this is the interval in which discrimination has proven most effective.

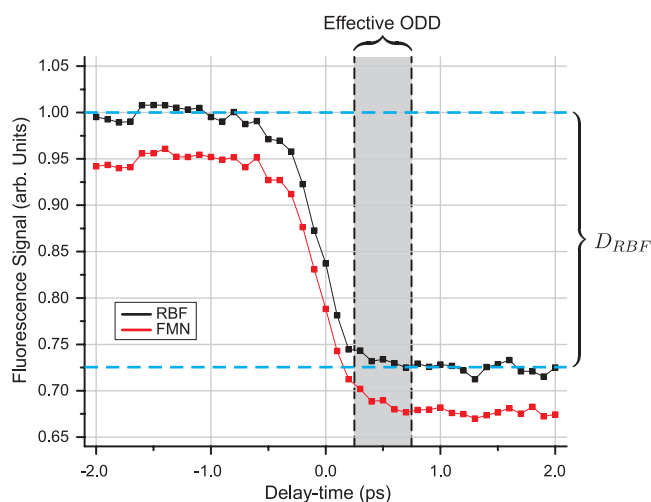


FIG. 7. Raw  $S_1$  fluorescence for RBF and FMN as a function of the delay time between the unshaped UV and IR pulses. The fluorescence depletion of FMN is offset by 5% for visual clarity. For delay times  $\tau \gtrsim 0$  ps the IR pulse depletes the  $S_1$  population by 15–30% depending on experimental conditions. ODD discrimination is performed within a delay of  $200 \lesssim \tau \lesssim 600$  (gray area). Simultaneous acquisition of RBF and FMN depletions ensures noise fluctuations are essentially equal and allows cancelation to first order.

### C. Learning control

In order to create distinguishable dynamic signatures for the two flavins, an optimal UV preparation pulse that maximizes the depletion ratio  $D_{\text{FMN}}/D_{\text{RBF}}$  is discovered through closed-loop, adaptive optimization of the fitness function  $J_1(\tau)$  at a fixed delay-time  $\tau$ :<sup>43</sup>

$$J_1(\tau) = D_{\text{FMN}}(\tau)/D_{\text{RBF}}(\tau) + 0.05D_{\text{RBF}}(\tau),$$

where  $D_{\text{FMN}}(\tau)/D_{\text{RBF}}(\tau) = 1.0$  indicates no discrimination afforded by the UV pulse. The first term of  $J_1(\tau)$  is the primary means for manipulating the flavin dynamics. The second bias term is necessary to prevent the evolutionary algorithm from introducing a linear spectral phase and thus time-shifting the UV pulse to follow the IR pulse, which would create meaningless depletion ratios. Likewise, the fitness function  $J_2(\tau) = D_{\text{RBF}}(\tau)/D_{\text{FMN}}(\tau) + 0.05D_{\text{FMN}}(\tau)$  is utilized for minimization of the depletion ratio  $D_{\text{FMN}}/D_{\text{RBF}}$ . Naturally, additional considerations or restrictions could be incorporated into the fitness functions (e.g., pulse shape simplicity,<sup>24</sup> robustness criteria,<sup>25</sup> etc.).

Each fitness function was maximized at a fixed delay time  $\tau$  under the direction of a genetic algorithm (GA).<sup>44</sup> The GA searches a 50 dimensional UV spectral phase space (which guarantees pulses of constant energy), where each phase pixel spans a domain of  $[0, 2\pi]$  with 5 bit resolution. The use of 50 pixels across the UV pulse bandwidth creates an effective shaper resolution of 0.222 nm/pixel and permits pulse shaping in a temporal window of  $\sim 5$  ps.<sup>13</sup> The GA employs a population size of 30 individuals, 2 cross-over points, 1 elitist, and a mutation probability of 0.25%. Henceforth, the presented data will regard the extremization of  $J_1(\tau)$  and  $J_2(\tau)$  as maximization and minimization of the depletion ratio  $D_{\text{FMN}}/D_{\text{RBF}}$ , respectively.

Any pulse-to-pulse variations in the focal volume or position that result from space–time coupling within the AOM pulse shaper<sup>45,46</sup> should affect both  $D_{\text{RBF}}$  and  $D_{\text{FMN}}$  equally; consequently, these spatial effects do not influence or bias the differential flavin depletion ratio  $D_{\text{FMN}}/D_{\text{RBF}}$ .

### V. EXPERIMENTAL RESULTS

Discrimination amongst the two flavins is enabled through concerted action of the two coherent fields working together in a nonlinear fashion to drive the molecular dynamics. To start, the specially shaped UV pulse at 400 nm coherently transfers population from the flavin ground state into a vibrational progression of the excited electronic states  $S_1$  or  $S_2$  (Fig. 4). Regardless of the specific temporal shape of this preparation pulse, any induced wavepacket in either flavin eventually decoheres whereupon relaxation to the ground state occurs by emission of spectrally identical, incoherent fluorescence photons. However, application of a time-delayed, unshaped pulse at 800 nm further excites the flavins to higher electronic states  $S_n$  primarily via two-photon absorption.<sup>3</sup> Irreversible depletion of the  $S_n$  manifold likely occurs through autoionizing states underlying the  $\sim 220$  nm absorption. Indeed, direct photoejection of electrons from the singlet manifold of aqueous-phase riboflavin has been ob-

served following application of 253.7 nm radiation.<sup>47,48</sup> Previous work has also established that  $\sim 30\%$  of the population excited into the  $S_n$  manifold is irreversibly lost to this depletion channel.<sup>3</sup> Accordingly, such a population depletion induced by the IR pulse results in a decreased fluorescence signal from the  $S_1$  state.

The degree of fluorescence depletion induced by this interrogation pulse depends upon the precise spatial and coherent character of the wavepackets at the IR pulse arrival time. It is also important to note that if the IR repump pulse is applied after the characteristic vibrational decoherence time (i.e.,  $\sim 2$  ps) but still within the fluorescence lifetime of  $S_1$  (i.e.,  $\sim 5$  ns), any transient, coherently driven dynamical distinctions amongst the two flavins is lost even though depletion is still observed. Accordingly, the shape of the UV pulse and the timing of the IR pulse should be considered as two aspects of a single coherent, two-color waveform working together to optimally drive the flavin excitation, relaxation, and depletion dynamics.

### A. Learning stage

Application of a transform-limited (TL) UV pulse followed by a time-delayed IR pulse results in indistinguishable flavin depletion signals for all times  $\tau$ . Specifically, the TL UV and time-delayed IR pulse induce statistically equivalent absolute depletions of  $\sim 21\%$  in both RBF and FMN (Fig. 8). This inseparability for all delay times  $\tau$  (see forthcoming discussion regarding Fig. 11) implies an equivalence of both nonlinear absorption cross sections and physical depletion mechanisms for RBF and FMN, which likely includes promotion to autoionizing states. Hence, the statistically identical nature of the depletions reflects an inability to discriminate with a properly delayed probe alone and necessitates control premised upon wavepacket dynamics.

Toward this end, the relative temporal populations of the  $S_1$  state for both flavins (measured with the depletion ratio  $D_{\text{FMN}}/D_{\text{RBF}}$ ) is utilized by ODD to induce a unique spatial and temporal wavepacket on each flavin's  $S_1$  potential energy surface that produces a discriminating difference upon arrival of the interrogating IR pulse. Random input phases result in highly unstable depletion signals with large error bars and an inability to offer reliable discrimination. Meaningful discrimination is only afforded upon stable convergence of the GA. Stability of the flavin depletion ratio induced by the TL pulse is crucial for the present control experiments,<sup>49</sup> and long-term signal-to-noise ratios are between 100 and 200 (Fig. 9).

As seen in Figs. 8 and 9, extremization of  $J(\tau)$  is able to discover a particular optimal UV pulse shape that in tandem with a properly delayed, unshaped IR pulse is able to effectively modulate the relative fluorescence ratio to favor either RBF or FMN. In particular, maximization of the depletion ratio  $D_{\text{FMN}}/D_{\text{RBF}}$  discovered a UV–IR pulse pair that yielded absolute depletions of  $D_{\text{RBF}} = 8.3\%$  and  $D_{\text{FMN}} = 12.2\%$  in Fig. 8(a). The absolute fluorescence depletions between RBF and FMN are now separated sufficiently to permit reliable discrimination. Likewise, minimization of  $D_{\text{FMN}}/D_{\text{RBF}}$  discovers a second UV pulse that while achieving approximately

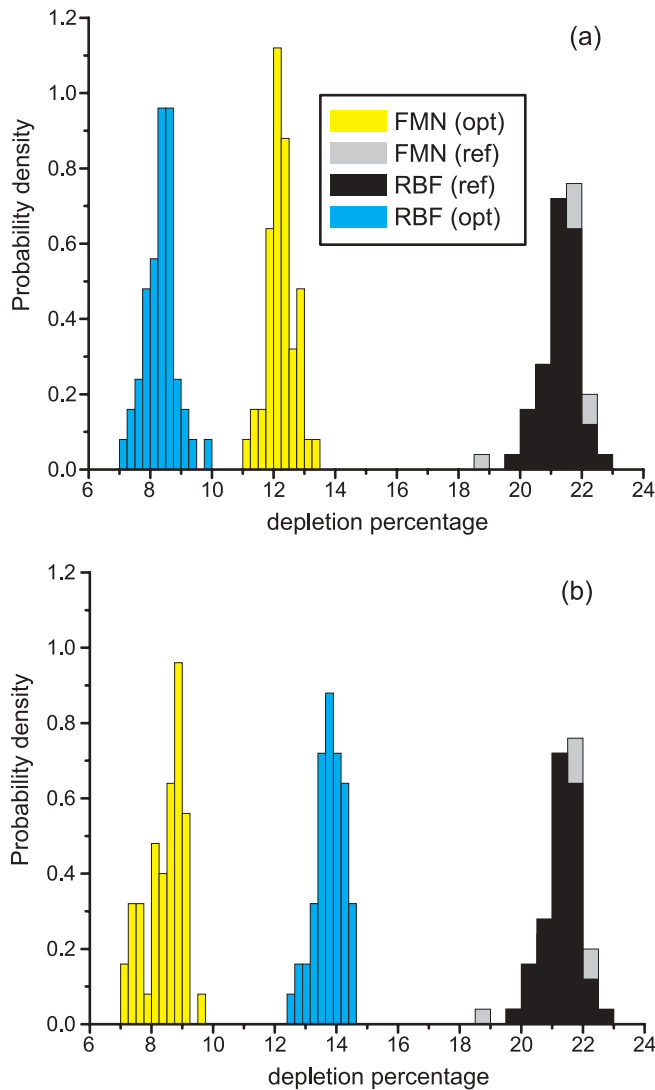


FIG. 8. Absolute RBF and FMN depletions for optimal UV pulse shapes at a time-delay of  $\tau = 500$  fs. Depletions induced by a TL UV pulse are statistically indistinguishable at  $\sim 21\%$ . Optimal UV pulses are discovered that dynamically maximize (a) and minimize (b) the two flavin depletions. This separation of absolute fluorescence depletions enables reliable discrimination through  $D_{FMN}/D_{RBF}$  as in Fig. 9(b).

the same level of discrimination, reverses the ordering of the flavin absolute depletions:  $D_{RBF} = 13.8\%$  and  $D_{FMN} = 8.4\%$  in Fig. 8(b).

The two systems are readily differentiated from one another by examination of the optimal depletion ratios  $D_{FMN}/D_{RBF}$  [Fig. 9(b)]. These optimal histograms possess a well-defined separation of  $\sim 84\%$  defined by 100 ( $\mu_{\max} - \mu_{\min}$ ), where  $\mu_{\max}$  and  $\mu_{\min}$  are the optimized depletions ratios  $D_{FMN}/D_{RBF}$  of 1.46 and 0.62, respectively. Hence, adaptive pulse shaping is able to separate the formerly unresolvable product channels. This separation is equivalently expressed as  $\sim 16\sigma$ , where  $(\mu_{\max} - \mu_{\min})/\sigma \simeq 16$  and  $\sigma = \sqrt{(\sigma_{\max}^2 + \sigma_{\min}^2)/2}$ ;  $\sigma_{\max}$  and  $\sigma_{\min}$  are the standard deviations corresponding to the optimal probability distributions displayed in Fig. 9(b). The desire for noise-robust solutions (i.e., narrow probability distributions) may also be included in the cost function.<sup>25</sup> Repeated optimizations observed vary-

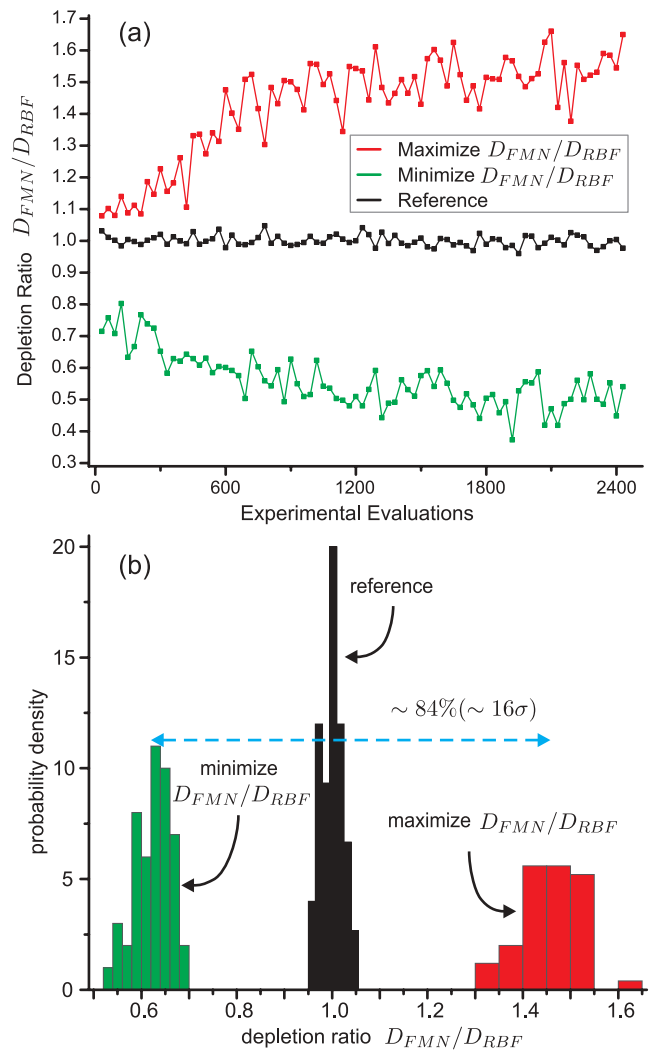


FIG. 9. Closed-loop, adaptive optimization of the flavin depletion ratio  $D_{FMN}/D_{RBF}$ . The GA discovers optimal UV pulses that maximize and minimize  $D_{FMN}/D_{RBF}$  (a). The depletion induced by the TL pulse is also displayed as a reference. Discovery of optimal UV pulse shapes enable a statistically significant separation between RBF and FMN of  $\sim 84\%$  ( $16\sigma$ ) (b). A histogram is constructed from 100 samples of 1000 averaged laser shots each.

ing distribution widths while yielding essentially identical degrees of discrimination; yet, there appears to be an inherent proclivity towards robust solutions.<sup>50</sup>

In order to better understand the transient nature of the optimized depletion process, Fig. 10 examines the flavin discrimination, originally optimized at  $\tau = 500$  fs, as the IR interrogation pulse delay time is scanned. As seen in Fig. 10, the UV control pulses fail to provide a separation of the depletion ratios for delay times longer than  $\sim 1$  ps. This time window is also consistent with the range of initial delay times  $\tau$  over which the GA can discover a discriminating pulse ( $\sim 200$ – $600$  fs as seen in Fig. 7). Since the first UV subpulse is consistently positioned at a time-delay of  $\sim -750$  fs (Fig. 12), the control process exhibits a coherence window of  $\sim 1.75$  ps. It is important to note that the delay time  $\tau$  in Figs. 10 and 11 is defined in terms of the unshaped UV pulse. Therefore, any statistically meaningful discrimination observed at delay times of  $\tau < 0$  fs originates from a component of the

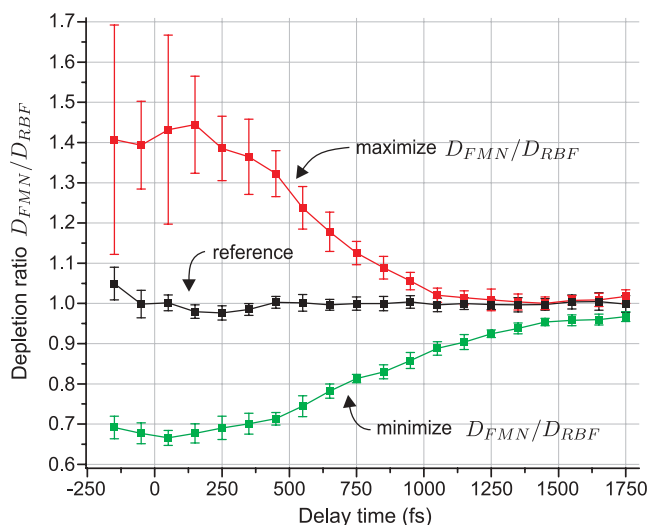


FIG. 10. Scan of the depletion ratio  $D_{FMN}/D_{RBF}$  as the delay time  $\tau$  is varied between an optimal UV pulse (optimized at  $\tau = 500$  fs) and an unshaped IR pulse. The temporal discrimination provided by the TL pulse is shown for reference. The optimal UV pulse enables significant discrimination for a temporal window of  $\sim 1.75$  ps. For delay times longer than this window, any vibrational coherence created by the shaped pulses is lost and the two flavins again exhibit identical depletion ratios.

shaped pulse that precedes the IR probe despite the negative delay time. Although each individual optimization may reveal a different control solution, the general behavior of Fig. 10 is consistently exhibited (i.e., a coherence window of  $< 2$  ps).

The fact that discrimination between RBF and FMN could not be achieved after a typical solution-phase vibrational decoherence time of  $\lesssim 2$  ps suggests the role of vibrational coherence in the underlying controlled dynamics. Indeed, rovibrational molecular coherences may persist for several picoseconds in the condensed phase prior to the onset of environmental-based decoherence.<sup>5</sup> In the case

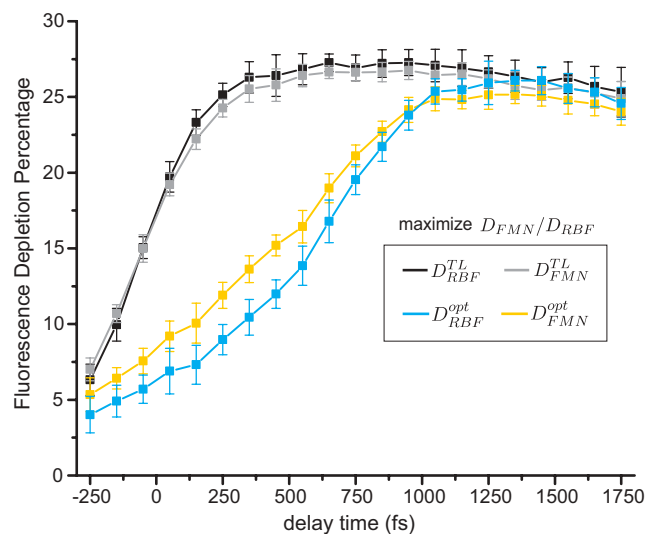


FIG. 11. Absolute RBF and FMN temporal depletions for maximization of the depletion ratio  $D_{FMN}/D_{RBF}$  as well as with the TL pulse. In order to separate the flavin dynamics, an optimal UV pulse lowers the absolute flavin depletions. After a delay time of  $\tau \sim 1$  ps, the individual flavin depletions return to their TL values, which indicates a loss of vibrational coherence and population relaxation. These absolute depletions correspond to the depletion ratio depicted in Fig. 10.

of riboflavin, intermolecular and solvent relaxation are observed to occur within  $\sim 1$  ps.<sup>32,51</sup> Within this time, coherent wavepacket motion involving several low-frequency ( $\lesssim 300$   $\text{cm}^{-1}$ ) vibrational modes of riboflavin solvated in water has been observed upon excitation with 400 nm pump pulses.<sup>51</sup> Transient absorption spectroscopy demonstrated that this coherent vibrational motion remains phased for several picoseconds, which agrees with the presently observed flavin discrimination window of  $\sim 1.75$  ps.

While temporal pulse overlap may be a feature of the control process, it is important to emphasize that the discrimination disappears after a delay of  $\tau \sim 1$  ps and not the physical fluorescence depletion, which is observable in both flavins for several nanoseconds. In fact, loss of discrimination is explained by the eventual return of both RBF and FMN depletions to their TL values after  $\tau \sim 1$  ps as seen in Fig. 11. It should be noted that the physical depletions depicted in Figs. 10 and 11 correspond to a different optimization experiment than those in Figs. 8 and 9. As expected, phase-only shaping of the UV pump pulse did not alter the overall population transfer efficiency in the absence of the interrogating IR pulse as seen in Fig. 11, and a return to the TL values reflects the ultimate decoherence and relaxation of the transient wavepackets. The incomplete return of the minimized depletion ratio in Fig. 10 is attributed to a gradual degradation of the pellicle beamsplitter throughout the course of the optimization.

Representative optimal UV pulses for both maximization and minimization of the depletion ratio  $D_{FMN}/D_{RBF}$  are shown as short-time Fourier transform spectrograms in Fig. 12. Each of the four rows depicts a unique UV pulse set

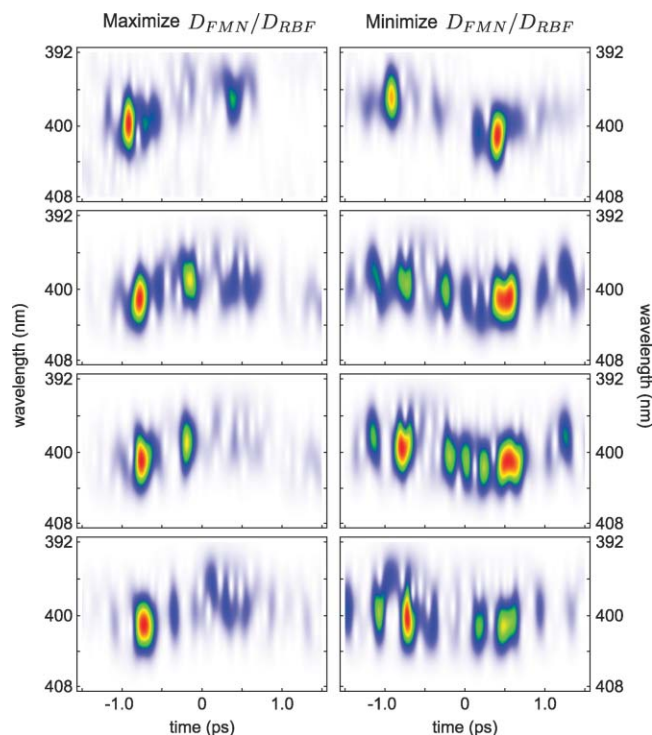


FIG. 12. Spectrograms of UV pulse pairs resultant from four distinct GA runs that alternatively maximize (left column) and minimize (right column) the flavin depletion ratio  $D_{FMN}/D_{RBF}$ . Each spectrogram is created with a short-time Fourier transform of the recovered SD-FROG fields.

discovered following a single deployment of the learning algorithm, where a single GA deployment consists of both maximization and minimization of  $D_{\text{FMN}}/D_{\text{RBF}}$ . Although each pulse set of the group provided nearly equivalent levels of discrimination, they varied in several fashions, including overall solution robustness, detailed temporal depletion and discrimination behavior (e.g., Fig. 10), and the degree that the physical depletions are lowered in order to obtain reliable discrimination (e.g., Figs. 8 and 11). The optimal UV pulse shapes contain multiple subpulses with varying temporal spacings and frequency distributions. For minimization of the depletion ratio  $D_{\text{FMN}}/D_{\text{RBF}}$ , the pulses consistently exhibit a frequency downchirp. Conversely, maximization of the depletion ratio produces pulses with the opposite chirp structure. Beyond this general chirp trend, a fair amount of variability exists among the subpulse patterns.

The presence of multiple subpulses within the optimal UV forms suggests a crucial role played by low-frequency vibrational resonances. Indeed, since the distinguishing structural variations amongst the two flavins arise in the ribityl chain, one might intuitively expect that the achieved discrimination manifests itself through control of the tail vibrational dynamics. The rigidity of the isoalloxazine ring along with the terminal side chain length results in a plethora of low-frequency torsional modes<sup>38</sup> that lie within the UV control pulse bandwidth ( $\Delta\lambda \simeq 220 \text{ cm}^{-1}$ ), which enables impulsive driving of their motion (i.e., the subpulse duration is considerably shorter than the vibrational period).<sup>52</sup>

A nascent understanding of the mechanism responsible for flavin discrimination may be gleaned through examination of the subpulse patterns and spacings depicted in Fig. 12. To start, a large degree of temporal correlation exists among the pulse intensities  $I_{\text{max}}(t)$  and  $I_{\text{min}}(t)$  that, respectively, maximize and minimize the depletion ratio  $D_{\text{FMN}}/D_{\text{RBF}}$  [correlation amongst a pair of optimal pulses is computed as  $C_t = \int_{-\infty}^{\infty} I_{\text{max}}(t)I_{\text{min}}(t)dt / (\sqrt{\int_{-\infty}^{\infty} I_{\text{max}}^2(t)dt} \sqrt{\int_{-\infty}^{\infty} I_{\text{min}}^2(t)dt})$ ]. For instance, the temporal correlations of the four pulse sets displayed in Fig. 12 are  $C_t = 0.75, 0.56, 0.66,$  and  $0.71$ . The considerable correspondence of temporal structure, especially among the strongest subpulses [e.g., Fig. 13(a)], has two important ramifications. First, the two optimal UV fields predominantly engage the same vibrational degrees of freedom and the resultant discrimination is dictated by the wavepacket phasing as derived from the UV temporal phase; consequently, the mechanism for modulating the depletion ratio likely relies on a short-lived coherence. Secondly, the temporal overlap suggests that the absolute delay of each subpulse with respect to the IR pulse is not random but instead repeatedly controlled so as to allow interruption of wavepacket evolution at a precise instant.

As a case study, we specifically examine the first pulse set of Fig. 12 (first row) since it is primarily composed of two UV subpulses [Fig. 13(a)]. The two subpulses contained in both optimal fields exhibit a spacing of  $\sim 24 \text{ cm}^{-1}$  ( $1.4 \text{ ps}$ ) as assessed by Fourier transforming the optimal UV intensity envelope,  $\tilde{I}(\omega) = (1/2\pi) \left| \int_{-\infty}^{\infty} I(t) \exp[i\omega t] dt \right|$ ; it is important to note that  $\tilde{I}(\omega)$  is not the power spectrum of the optimal field, which is independent of the spectral phase. Subpulses

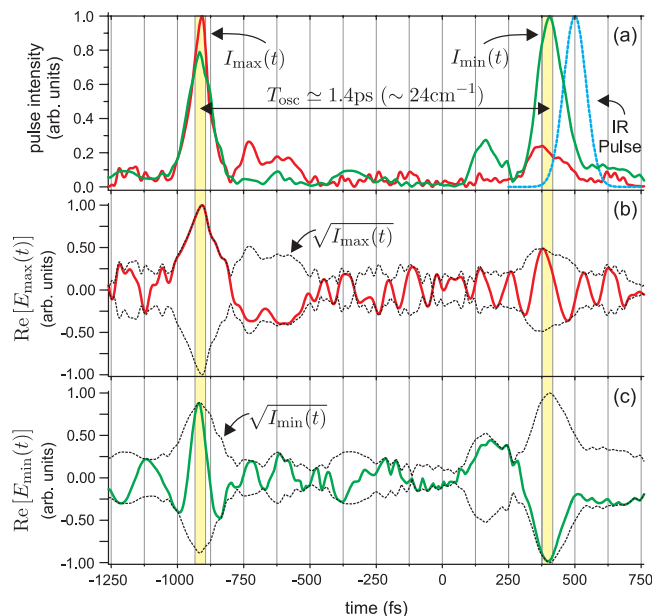


FIG. 13. SD-FROG retrieved optimal UV fields corresponding to the first pulse set of Fig. 12. Considerable temporal overlap of  $I_{\text{max}}(t)$  and  $I_{\text{min}}(t)$  is observed (a), which suggests that both fields engage a common vibrational mode and the resultant discrimination is dependent upon the relative subpulse phasing. Examination of  $\text{Re}[E_{\text{max}}(t)]$  reveals an in-phase subpulse structure (b) while  $\text{Re}[E_{\text{min}}(t)]$  exhibits an antiphased sequence (c). In both panels (b) and (c), the slowly varying temporal envelope  $\sqrt{I(t)}$  is shown for reference. High-frequency oscillations in (a) result from noise in the FROG inversion procedure.

spaced at a target vibrational period have been shown to form a natural discriminatory pulse sequence for identification of polyatomic normal modes of vibration.<sup>52–54</sup> In the present circumstance, the first subpulse of each UV sequence initializes wavepacket propagation on the first excited electronic surface  $S_1$  of each flavin. Contingent upon the relative phase  $\Delta\phi$  and amplitude of the second subpulse, constructive or destructive interference may be induced for vibrational modes with a classical oscillatory period  $T_{\text{osc}}$  that matches the experimental subpulse temporal spacing. Correspondingly, the spatial localization of the resultant wavepacket can either enhance or diminish the coupling efficiency to higher electronic states with the IR pulse.

In the case of  $I_{\text{max}}(t)$ , the relative phase between these two subpulses is  $\Delta\phi_{\text{max}} \simeq 0.05\pi$  [Fig. 13(b)]. Thus, the second subpulse appears to constructively reinforce spatial localization of the  $\sim 24 \text{ cm}^{-1}$  wavepacket in the  $S_1$  state, whereupon immediate re-excitation to higher electronic states by the IR pulse is enhanced.<sup>55</sup> Contrarily, the two nearly equal intensity subpulses of  $I_{\text{min}}(t)$  exhibit a relative phase of  $\Delta\phi_{\text{min}} \simeq 0.86\pi$  [Fig. 13(c)]. These antiphased subpulses deconstruct the vibrational wavepacket, and thus overlap between the  $S_1$  state and higher electronic states is diminished, which likewise decreases fluorescence depletion of the flavin  $S_1$  state. It is also worth noting that the two antiphased subpulses of  $I_{\text{min}}(t)$  are of nearly equal intensity in order to achieve increased cancellation of the wavefunction in this particular normal mode of  $S_1$ ; constructive reinforcement of the wavefunction takes place for any ratio of subpulse intensities. Accordingly, the control mechanism is inferred to be a

variant of wavepacket interferometry<sup>52,56,57</sup> induced by a phase-locked intrapulse pair (phase-locking here refers to a constant phase relationship between various subpulses of the temporal envelope). Within a few picoseconds, energy flows across the entire molecular framework [intramolecular vibrational energy redistribution (IVR)<sup>58</sup>] and redistributes the initially localized vibrational excitation; hence, the controlled interference is destroyed and differences in the coupling to higher electronic states are eliminated (e.g., Figs. 10 and 11).

Since constructive interference is achieved for the UV pulse that maximizes the depletion ratio  $D_{\text{FMN}}/D_{\text{RBF}}$ , the controlled  $\sim 24 \text{ cm}^{-1}$  vibrational mode is inferred to belong to FMN. The increased mass of the  $\text{PO}_4$  group likely sufficiently separates torsional-type motion of the entire FMN ribityl chain from the corresponding mode in RBF, which makes it an attractive candidate for a discriminatory phase-locked pulse sequence.

The optimal UV spectral phases corresponding to the fields shown in Fig. 13 are depicted in Fig. 14 (the spectral phases retrieved by SD-FROG match the phase pattern placed on the AOM). The evolutionary algorithm crafts two subpulses through construction of triangle-like spectral phases of opposite sign (a linear phase temporally shifts one half of the spectrum in a given time direction while a negated linear phase shifts the other half in an opposite direction). A spectral phase jump of  $\pi$  is readily apparent at  $\sim 398.5 \text{ nm}$  for  $\phi_{\text{min}}(\lambda)$  in order to generate the antiphased pulse sequence that minimizes the depletion ratio  $D_{\text{FMN}}/D_{\text{RBF}}$  [Fig. 14(b)]. Variations upon this general triangle structure are evident for all the optimal spectral phases associated with the spectrograms of Fig. 12.

The consistent convergence to a frequency upchirp for the subpulse pair that maximizes the depletion ratio  $D_{\text{FMN}}/D_{\text{RBF}}$  and a frequency downchirp for minimization of the depletion ratio may have several explanations. The Franck–Condon region of the  $S_1$  potential energy hypersur-

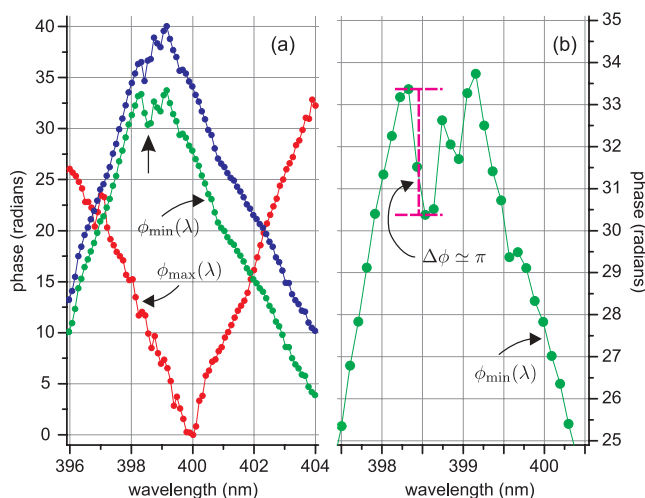


FIG. 14. SD-FROG retrieved optimal UV spectral phases corresponding to the fields shown in Fig. 13. Each spectral phase exhibits a triangle-like pattern (a), which creates the observed two subpulses spaced at  $\sim 1.4 \text{ ps}$ . A phase discontinuity of  $\sim \pi$  is also evident in  $\phi_{\text{min}}(\lambda)$  (b) in order to craft the antiphased subpulses of  $I_{\text{min}}(t)$ . For comparison,  $\phi_{\text{min}}(\lambda)$  with the  $\pi$  discontinuity removed at  $\sim 398.5 \text{ nm}$  is also displayed (blue) in panel (a).

face lies far from the equilibrium molecular geometry following excitation with 400 nm radiation (the  $0 \rightarrow 0$  band is  $\sim 475 \text{ nm}$ ). This initial compression is presumably quite important for the low-frequency torsional modes of the ribityl chain where vibronic anharmonicities may be significant. Hence, for the situation in which wavepacket localization is desirable [Fig. 13(b)], an initial launch composed of lower-energy eigenstates instills a “reflectron” character<sup>59,60</sup> on to the generated wavepacket, whereupon it is constructively amplified when returning to the Franck–Condon region. Conversely, an initial launch of higher-energy vibrational eigenstates imparts a “cannon” character<sup>59,60</sup> on to the outgoing wavepacket, which results in slightly degraded localization upon returning to the Franck–Condon window. It is also possible that the observed chirp structure is a result of phase-only modulation, and various other structures, including replica double pulses with the appropriate intrapulse phase relation, would be obtained if amplitude modulation was included in the optimization routine.

While wavepacket interferometry of essentially a single vibrational degree of freedom can produce statistically significant separations of the flavin depletions [the UV pulse set shown in Fig. 13 results in  $\mu_{\text{max}} - \mu_{\text{min}} \sim 0.44(15\sigma)$ ], higher fidelity control is afforded upon concomitant control of several normal modes present in both RBF and FMN. For instance, a subpulse spacing of  $\sim 50 \text{ cm}^{-1}$  ( $\sim 663 \text{ fs}$ ) is especially prominent in  $I_{\text{max}}(t)$  and  $I_{\text{min}}(t)$  of the second and third pulse sets in Fig. 12. During maximization of the depletion ratio  $D_{\text{FMN}}/D_{\text{RBF}}$ , this pulse pair of nearly equal intensity is antiphased ( $\Delta\phi \sim \pi$ ) while the already discussed  $\sim 24 \text{ cm}^{-1}$  subpulse pair of  $I_{\text{min}}(t)$  retains its antiphased relation ( $\Delta\phi \sim \pi$ ) (see Appendix). Since the UV control pulse that maximizes the depletion ratio achieves destructive interference for  $T_{\text{osc}} \simeq 663 \text{ fs}$  ( $\sim 50 \text{ cm}^{-1}$ ), this mode is presumed to be torsional-type motion of the RBF ribityl side chain. This inferred RBF normal mode at  $\sim 50 \text{ cm}^{-1}$  agrees well with the observed 298 K far-IR spectrum of RBF, which exhibits two strong, well-resolved ribityl torsional modes at 50.7 and 64.3  $\text{cm}^{-1}$ .<sup>38</sup> Accordingly, this particular pulse set contains pulse sequences that simultaneously exert impulsive control over vibrations of both RBF and FMN in order to manipulate the depletion ratio  $D_{\text{FMN}}/D_{\text{RBF}}$  and achieve slightly enhanced flavin discrimination [the third pulse set results in  $\mu_{\text{max}} - \mu_{\text{min}} \sim 0.56(12\sigma)$ ].

The existence of several distinct UV phase-locked intrapulse sequences that achieve an equivalent depletion ratio reaffirms the notion of multiple, equally successful, unique control pulses for a given problem.<sup>61</sup> For instance, the success of each optimization does not generally depend upon the level of fluorescence depletion, which itself varies with the IR pulse intensity, and each pulse pair in Fig. 12 was discovered while interacting with a different IR pulse intensity. Thus, while the IR pulse intensity determines the overall flavin depletion, each optimization discovers a unique UV–IR pulse pair that provides approximately the same degree of control over the depletion ratio  $D_{\text{FMN}}/D_{\text{RBF}}$ . Yet while each pulse pair of Fig. 12 is distinct, a fair degree of correlation (defined through  $C_I$ ) exists in the underlying subpulse sequences within each column. Such solution multiplicity permits considerable

flexibility in selecting a suitable optimal field when presented with limited control resources.

It is also worth noting that several of the optimal pulses evince temporal structure with a nonintuitive role in the controlled dynamics. Indeed, such structure on a given pulse, which is generally high frequency, does not contribute to the aforementioned temporal overlap  $C_t$ , and it is unknown whether it plays a genuine role in achieving the desired flavin discrimination or is simply a side effect of creating the necessary intensity profile with phase-only shaping.

The inadequacy of the TL pulse for discrimination stems from its simultaneous excitation of all vibrational motion for both RBF and FMN, of which the vast majority is practically identical. Hence, tiny variations due to unique motions of the ribityl side chain are obscured by the stronger, indistinguishable ring motions. However, the use of properly phased, impulsive pulse sequences resonant with the vibrational periods of these low-frequency, distinguishing tail modes permits their recognition and amplifies their signature.

## B. Discrimination stage

ODD additionally provides a novel means for quantitative detection in demanding circumstances, such as measuring the presence of flavins after having assembled a set of UV pulses effective at differentiating RBF and FMN. The overlapping fluorescence spectra of RBF and FMN typically precludes the use of conventional luminescence spectroscopies for determination of the individual concentrations in a mixture containing both flavins. Such an assay would be useful, for instance, with *in vivo* monitoring of metabolic activity. Whereas steady-state spectroscopies fail to generate discernable differences, a set of optimal UV–IR pulse pairs may be utilized to generate unique dynamical responses of each flavin and thus provide the basis for independent, quantitative detection.

In particular, the absolute depleted fluorescence signals (relative depletion signals are concentration independent) for 53.7 and 52.6  $\mu\text{M}$  pure solutions of RBF and FMN, respectively, are measured when exposed to a collection of previously discovered optimal UV–IR pulse pairs. The depleted fluorescence signal from a flavin mixture exposed to the same pulse set may then be related to its fractional components with the following equation:

$$F_{\text{mix},n} = c_{\text{RBF}} F_{\text{RBF},n}^{\text{d}} + c_{\text{FMN}} F_{\text{FMN},n}^{\text{d}}, \quad (2)$$

where  $F_{\text{RBF},n}^{\text{d}}$  and  $F_{\text{FMN},n}^{\text{d}}$  are the absolute depleted fluorescence signals from pure solutions of RBF and FMN, respectively, and  $0 \leq c_{\text{RBF}}, c_{\text{FMN}} \leq 1$  (the constraint  $c_{\text{RBF}} + c_{\text{FMN}} = 1$  was not utilized in the present circumstance). Depleted fluorescence signals from both pure solutions and the mixture are measured in a single flow cell to ensure identical experimental conditions. The relative delay between the UV and IR pulse pair is set to the same value used during the optimization stage (or to a delay that provides maximal discrimination as assessed by examining  $D_{\text{FMN}}/D_{\text{RBF}}$  as a function of delay  $\tau$ ). Finally, all signals are obtained by collecting 300 samples where each sample consists of 1000 averaged laser shots in

TABLE I. Discrimination experiments for independent determination of RBF and FMN concentrations in a mixture. Although two experiments could reveal the flavin concentrations within statistical uncertainty (rows 1 and 2), overdetermination of Eq. (2) by measuring the depleted fluorescence at multiple UV–IR delay times  $\tau$  significantly reduces the uncertainty of the retrieved concentrations (row 3).

Experiments	$c_{\text{RBF}}^{\text{true}}, c_{\text{FMN}}^{\text{true}}$	$c_{\text{RBF}}^{\text{meas}}$	$c_{\text{FMN}}^{\text{meas}}$
2	0.30, 0.70	$0.24 \pm 0.10$	$0.82 \pm 0.19$
2	0.50, 0.50	$0.55 \pm 0.07$	$0.47 \pm 0.09$
11	0.33, 0.66	$0.36 \pm 0.03$	$0.66 \pm 0.03$

order to accrue both the mean and standard deviation of depleted fluorescence signals corresponding to a single UV–IR pulse pair.

A minimum of two distinct pulse pairs is required for retrieval of the individual flavin concentrations, and typical results of this procedure are illustrated in Table I. While working with the minimum number of measurements generally allowed for determination of RBF and FMN fractional mixture concentrations, the underlying concentration uncertainties could be large. However, the concentration retrieval problem is readily overdetermined through observation of the absolute depletions for both RBF and FMN when subjected to an optimal UV pulse with variable IR pulse delay. In this manner, the retrieval equation is overdetermined by measuring the fluorescence depletion of each solution for a variety of UV–IR pulse delay times  $\tau$ . Observation of flavin dynamics through the use of such time series data mitigates the presence of noise both in the laser system as well as the detector and is thus able to provide enhanced quantitative discrimination.<sup>62</sup> Delay times are chosen for which RBF and FMN exhibit distinct dynamic responses for an optimal UV pulse shape as in Fig. 11. Accordingly, the depleted fluorescence of each solution is recorded at delay times of  $\tau = 250, 375, 400, 500, 600, \text{ and } 700$  fs for each of the two optimal pulses that maximize and minimize the depletion ratio  $D_{\text{FMN}}/D_{\text{RBF}}$ . Least squares minimization is then utilized to linearly regress the data (Fig. 15) and obtain the flavin concentrations displayed in Table I.

The generation of additional linearly independent data through time series measurement greatly reduces the uncertainty of the retrieved flavin fractional concentrations. While not explicitly performed here, the existence of multiple control solutions could also be directly used to overdetermine the retrieval equation and may be crucial for reliable identification of similar molecules. Finally, the incorporation of robustness goals directly into the fitness functional<sup>25</sup> may aid in minimizing the measurement time and enhancing the quality of the fractional concentrations. No attempt was made to push the detection limit of the technique, and the depleted fluorescence signals were easily recorded for concentrations approaching the physiologically relevant micromolar level.

## VI. CONCLUSION

In summary, an optimally shaped UV femtosecond pulse followed by an appropriately delayed IR pulse are able

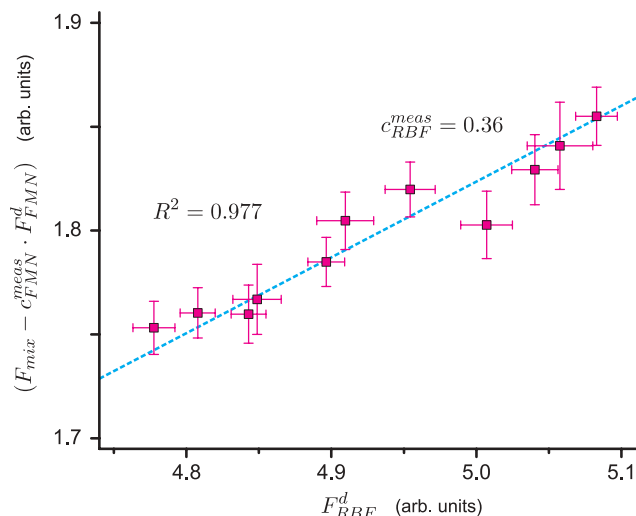


FIG. 15. Experimentally measured depleted fluorescence signals for both a pure solution of RBF and a solution containing a mixture of both RBF and FMN. Linearly independent data are obtained by recording the fluorescence signals as the delay time  $\tau$  between the optimal UV and IR pulses is varied. The extracted slope of 0.36 is the fractional context,  $c_{RBF}^{meas}$ , of RBF reported in the third row of Table I.

to provide significant dynamic discrimination amongst two, condensed-phase compounds that are practically indistinguishable when examined with linear, steady-state spectroscopic methods. Slight variations in the vibrational structure which are not plainly visible in the static spectra of Fig. 3 can be dynamically amplified through optimal control.

Although the control UV pulse possesses a modest  $\sim 3.5$  nm of bandwidth, the attained dynamic selectivity is nonetheless profound and enables reliable, statistically significant discrimination. Through impulsive, intrapulse phase-locked sequences, wavepacket motion of discriminating, low-frequency ribityl torsional modes is coherently controlled, and judicious control of wavepacket interferences either enhances or diminishes the subsequent coupling efficiency to irreversible higher electronic states by the IR pulse. An increase in control bandwidth at 400 nm should significantly increase the number of accessible low-frequency isoalloxazine ring vibrations and ribityl torsional modes that may be driven impulsively, which in turn may greatly increase the finesse and magnitude of the attained control.

Rather than being a hindrance, the large number of vibrational degrees of freedom possessed by complex molecular entities eases discovery of a suitable vibrational mode that permits discrimination with the available control bandwidth. Hence, significant control of complex systems appears feasible for a variety of applications, including the use of ODD techniques in demanding recognition and detection circumstances.

The success of ODD in transiently removing the indistinguishability of RBF and FMN linear spectra also permits use of the technique for quantitative analytical applications. With a properly chosen UV pulse form, the two flavins exhibit statistically distinct temporal depletions within their coherence time, and this variation in transient response permitted reliable retrieval of the fractional flavin concentrations. Such an

analytical technique may prove useful for nondestructive, *in vivo* optical imaging of biological fluorophores that exhibit overlapping, diffuse molecular spectra as well as other analogous applications.

The activation and regulation of proteins and biomolecules via phosphorylation of particular amino acid subunits is ubiquitous in cellular biology, and the potential for discrimination between phosphorylated and unphosphorylated forms via ODD presents many opportunities for *in vivo* investigation. For instance, tyrosine phosphorylation is responsible for mediation of cellular insulin receptors and initiation of signal transduction pathways. As is the case with the flavins, both tyrosine and its phosphorylated counterpart, phosphotyrosine, exhibit nearly identical linear absorbance and fluorescence spectra, and thus are a fine candidate for ODD.<sup>63</sup>

Quantum control is ultimately a matter of discrimination amongst multifarious product channels, whether they be competitive channels of a single system or strikingly similar channels shared by multiple systems. While low-resolution control has been convincingly demonstrated, the ability of pulse shaping techniques to achieve high fidelity control amongst product channels of ever-increasing similarity has been largely untested. As a demonstration of such capability, ODD has permitted demarcation of product channels unresolvable without optimal pulse shaping.

In conclusion, ODD offers a new variation of dynamic spectroscopy for detection based upon the transient separation and enhancement of minute steady-state spectral differences. The attainment of high-finesse product channel control in complex systems bodes well for future ODD development and the possibility to likewise obtain high fidelity product distinction in various demanding control applications.

## ACKNOWLEDGMENTS

J.-P.W. and F.C. acknowledge support from the Swiss National Science Foundation. H.R. acknowledges support from DHS, ONR, and ARO.

## APPENDIX: SUPPLEMENTAL OPTIMAL FIELDS

An additional optimal UV field is displayed in Fig. 16 in order to further reinforce the inferred mechanism of intrapulse, phase-locked pulse sequences. As discussed above, this particular  $I_{max}(t)$ , which corresponds to the second pulse set of Fig. 12, is also primarily composed of two subpulses. The subpulse pair possesses a  $T_{osc} \simeq 663$  fs ( $\sim 50$  cm<sup>-1</sup>) spacing and displays an antiphased relation as seen in Fig. 16(a). Since this field is responsible for an increase in the flavin depletion ratio  $D_{FMN}/D_{RBF}$ , it is surmised that this spacing resonantly drives a torsion-type normal mode of the RBF ribityl side chain in a destructive manner. This inferred normal mode frequency of RBF corresponds well with the 298 K THz vibrational spectrum of riboflavin, which reveals prominent RBF ribityl torsion modes at 50.7 and 64.3 cm<sup>-1</sup>.<sup>38</sup> As with Fig. 14, the optimal spectral phase  $\phi_{max}(\lambda)$  reveals a general triangle-like pattern [Fig. 16(b)] in order to construct the observed subpulse spacing; a  $\pi$  discontinuity in  $\phi_{max}(\lambda)$  is

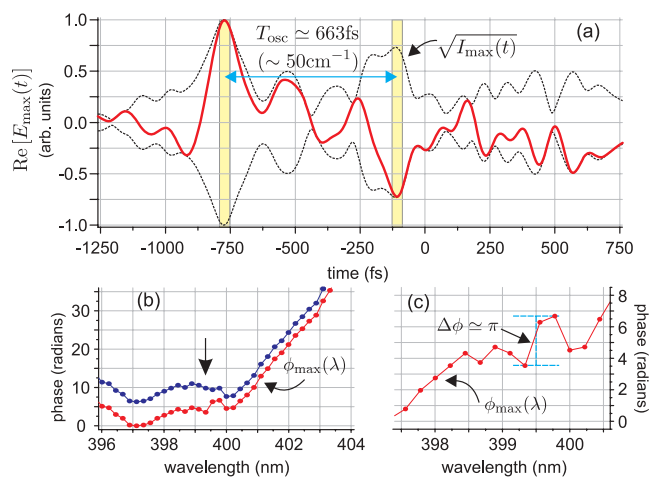


FIG. 16. Optimal UV field for maximization of the depletion ratio that corresponds to the second pulse set of Fig. 12. The subpulse sequence with a  $\sim 50 \text{ cm}^{-1}$  spacing exhibits an antiphased relationship (a). The optimal spectral phase again expresses a triangle-like pattern (b) with a noticeable phase discontinuity of  $\sim \pi$  at  $\sim 399.5 \text{ nm}$  (c). For comparison, the optimal phase with the  $\pi$  discontinuity removed is also displayed (blue) in panel (b). The slowly varying temporal envelope  $\sqrt{I_{\max}(t)}$  is shown in (a) for reference.

additionally evident as seen in Fig. 16(c). This phase discontinuity is responsible for the optimal antiphased pulse sequence in Fig. 16(a).

<sup>1</sup>F. Courvoisier, L. Bonacina, V. Boutou, L. Guyon, C. Bonnet, B. Thuillier, J. Extermann, M. Roth, H. Rabitz, and J. P. Wolf, *Faraday Discuss.* **137**, 37 (2008).  
<sup>2</sup>F. Courvoisier, V. Boutou, V. Wood, A. Bartelt, M. Roth, H. Rabitz, and J. P. Wolf, *Appl. Phys. Lett.* **87**, 063901 (2005).  
<sup>3</sup>F. Courvoisier, L. Bonacina, V. Boutou, L. Guyon, C. Bonnet, B. Thuillier, J. Extermann, M. Roth, H. Rabitz, and J. P. Wolf, *J. Photochem. Photobiol., A* **180**, 300 (2006).  
<sup>4</sup>H. Rabitz, R. de Vivie-Riedle, M. Motzkus, and K. Kompa, *Science* **288**, 824 (2000).  
<sup>5</sup>P. Nuernberger, G. Vogt, T. Brixner, and G. Gerber, *Phys. Chem. Chem. Phys.* **9**, 2470 (2007).  
<sup>6</sup>C. Daniel, J. Full, L. Gonzalez, C. Lupulescu, J. Manz, A. Merli, S. Vajda, and L. Woste, *Science* **299**, 536 (2003).  
<sup>7</sup>E. Wells, K. Betsch, C. Conover, M. DeWitt, D. Pinkham, and R. Jones, *Phys. Rev. A* **72**, 063406 (2005).  
<sup>8</sup>B. Sussman, D. Townsend, M. Ivanov, and A. Stolow, *Science* **314**, 278 (2006).  
<sup>9</sup>R. Bartels, S. Backus, E. Zeek, L. Misoguti, G. Vdovin, I. Christov, M. Murnane, and H. Kapteyn, *Nature* **406**, 164 (2000).  
<sup>10</sup>T. Laermann, I. Shchatsinin, A. Stalmashonak, M. Boyle, N. Zhavoronkov, J. Handt, R. Schmidt, C. P. Schulz, and I. V. Hertel, *Phys. Rev. Lett.* **98**, 058302 (2007).  
<sup>11</sup>V. I. Prokhorenko, A. M. Nagy, S. A. Waschuk, L. S. Brown, R. R. Birge, and R. Miller, *Science* **313**, 1257 (2006).  
<sup>12</sup>D. G. Kuroda, C. P. Singh, Z. Peng, and V. D. Kleiman, *Science* **326**, 263 (2009).  
<sup>13</sup>A. Weiner, *Rev. Sci. Instrum.* **71**, 1929 (2000).  
<sup>14</sup>S. Backus, C. G. D. III, M. M. Murnane, and H. C. Kapteyn, *Rev. Sci. Instrum.* **69**, 1207 (1998).  
<sup>15</sup>T. Bäck, *Evolutionary Algorithms in Theory and Practice* (Oxford University, New York, 1996).  
<sup>16</sup>T. Brixner, N. Damrauer, P. Niklaus, and G. Gerber, *Nature* **414**, 57 (2001).  
<sup>17</sup>B. Schaefer-Bung, V. Bonacic-Koutecky, F. Sauer, S. M. Weber, L. Woeste, and A. Lindinger, *J. Chem. Phys.* **125**, 214310 (2006).  
<sup>18</sup>E. R. Tkaczyk, A. H. Tkaczyk, K. Mauring, J. Y. Ye, J. R. Baker, Jr., and T. B. Norris, *J. Lumin.* **130**, 29 (2010).

<sup>19</sup>B. Li, G. Turinici, V. Ramakrishna, and H. Rabitz, *J. Phys. Chem. B* **106**, 8125 (2002).  
<sup>20</sup>G. Turinici, V. Ramakrishna, B. Li, and H. Rabitz, *J. Phys. A* **37**, 273 (2004).  
<sup>21</sup>M. Roth, L. Guyon, J. Roslund, V. Boutou, F. Courvoisier, J. P. Wolf, and H. Rabitz, *Phys. Rev. Lett.* **102**, 253001 (2009).  
<sup>22</sup>B. Li, W. Zhu, and H. Rabitz, *J. Chem. Phys.* **124**, 024101 (2006).  
<sup>23</sup>J. Geremia, W. Zhu, and H. Rabitz, *J. Chem. Phys.* **113**, 10841 (2000).  
<sup>24</sup>A. Lindinger, S. Weber, C. Lupulescu, F. Vetter, M. Plewicki, A. Merli, L. Woste, A. Bartelt, and H. Rabitz, *Phys. Rev. A* **71**, 013419 (2005).  
<sup>25</sup>A. Bartelt, M. Roth, M. Mehendale, and H. Rabitz, *Phys. Rev. A* **71**, 063806 (2005).  
<sup>26</sup>P. Heelis, *Chem. Soc. Rev.* **11**, 15 (1982).  
<sup>27</sup>J. Eweg, F. Muller, A. Visser, C. Veeger, D. Bebelaar, and J. VanVoorst, *Photochem. Photobiol.* **30**, 463 (1979).  
<sup>28</sup>P. Dutta and T. Spiro, *J. Chem. Phys.* **69**, 3119 (1978).  
<sup>29</sup>T. Schuttrigkeit, C. Kompa, M. Salomon, W. Rudiger, and M. Michel-Beyerle, *Chem. Phys.* **294**, 501 (2003).  
<sup>30</sup>R. J. Stanley and H. Jang, *J. Phys. Chem. A* **103**, 8976 (1999).  
<sup>31</sup>H. A. Harbury, K. F. LaNoue, P. A. Loach, and R. M. Amick, *Proc. Natl. Acad. Sci. U.S.A.* **45**, 1708 (1959).  
<sup>32</sup>S. Islam, A. Penzkofer, and P. Hegemann, *Chem. Phys.* **291**, 97 (2003).  
<sup>33</sup>P. Drossler, W. Holzer, A. Penzkofer, and P. Hegemann, *Chem. Phys.* **282**, 429 (2002).  
<sup>34</sup>C. Neiss, P. Saalfrank, M. Parac, and S. Grimme, *J. Phys. Chem. A* **107**, 140 (2003).  
<sup>35</sup>M. Kowalczyk, E. Sikorska, I. Khmelinskii, J. Komasa, M. Insinska-Rak, and M. Sikorski, *J. Mol. Struct.: THEOCHEM* **756**, 47 (2005).  
<sup>36</sup>M. Abe, Y. Kyogoku, T. Kitagawa, K. Kawano, N. Ohishi, A. Takaisuzuki, and K. Yagi, *Spectrochim. Acta, Part A* **42**, 1059 (1986).  
<sup>37</sup>M. Wolf, C. Schumann, R. Gross, T. Domratheva, and R. Diller, *J. Phys. Chem. B* **112**, 13424 (2008).  
<sup>38</sup>M. Takahashi, Y. Ishikawa, J. Nishizawa, and H. Ito, *Chem. Phys. Lett.* **401**, 475 (2005).  
<sup>39</sup>J. Tull, M. Dugan, and W. Warren, *Advances in Magnetic & Optical Resonance* (Academic, New York, 1997), Vol. 20.  
<sup>40</sup>M. Roth, M. Mehendale, A. Bartelt, and H. Rabitz, *Appl. Phys. B* **80**, 441 (2005).  
<sup>41</sup>Y. Pan, R. Pinnick, S. Hill, S. Niles, S. Holler, J. Bottiger, J. P. Wolf, and R. Chang, *Appl. Phys. B* **72**, 449 (2001).  
<sup>42</sup>W. Holzer, J. Shirdel, P. Zirk, A. Penzkofer, P. Hegemann, R. Deutzmann, and E. Hochmuth, *Chem. Phys.* **308**, 69 (2005).  
<sup>43</sup>R. Judson and H. Rabitz, *Phys. Rev. Lett.* **68**, 1500 (1992).  
<sup>44</sup>B. Pearson, J. White, T. Weinacht, and P. Bucksbaum, *Phys. Rev. A* **63**, 063412 (2001).  
<sup>45</sup>F. Frei, A. Galler, and T. Feurer, *J. Chem. Phys.* **130**, 034302 (2009).  
<sup>46</sup>N. Krebs, R. A. Probst, and E. Riedle, *Opt. Express* **18**, 6164 (2010).  
<sup>47</sup>N. Getoff, S. Solar, and D. McCormick, *Science* **201**, 616 (1978).  
<sup>48</sup>C. Lu, W. Wang, W. Lin, Z. Han, S. Yao, and N. Lin, *J. Photochem. Photobiol., B* **52**, 111 (1999).  
<sup>49</sup>M. Roth, J. Roslund, and H. Rabitz, *Rev. Sci. Instrum.* **77**, 083107 (2006).  
<sup>50</sup>H. Rabitz, *Phys. Rev. A* **66**, 063405 (2002).  
<sup>51</sup>A. Weigel, A. Dobryakov, M. Veiga, and J. Lustres, *J. Phys. Chem. A* **112**, 12054 (2008).  
<sup>52</sup>A. Weiner, D. Leaird, G. Wiederrecht, and K. Nelson, *Science* **247**, 1317 (1990).  
<sup>53</sup>N. Dudovich, D. Oron, and Y. Silberberg, *J. Chem. Phys.* **118**, 9208 (2003).  
<sup>54</sup>W. Pollard, S. Dexheimer, Q. Wang, L. Peteanu, C. Shank, and R. Mathies, *J. Phys. Chem.* **96**, 6147 (1992).  
<sup>55</sup>K. Ohmori, H. Katsuki, H. Chiba, M. Honda, Y. Hagihara, K. Fujiwara, Y. Sato, and K. Ueda, *Phys. Rev. Lett.* **96**, 093002 (2006).  
<sup>56</sup>N. Scherer, R. Carlson, A. Matro, M. Du, A. Ruggiero, V. Romerorochin, J. Cina, G. Fleming, and S. Rice, *J. Chem. Phys.* **95**, 1487 (1991).  
<sup>57</sup>J. Voll and R. de Vivie-Riedle, *New J. Phys.* **11**, 105036 (2009).  
<sup>58</sup>D. Nesbitt and R. Field, *J. Phys. Chem.* **100**, 12735 (1996).  
<sup>59</sup>J. Krause, R. Whitnell, K. Wilson, Y. Yan, and S. Mukamel, *J. Chem. Phys.* **99**, 6562 (1993).  
<sup>60</sup>J. Cao and K. Wilson, *J. Chem. Phys.* **107**, 1441 (1997).  
<sup>61</sup>J. Roslund, M. Roth, and H. Rabitz, *Phys. Rev. A* **74**, 043414 (2006).  
<sup>62</sup>B. Li, H. Rabitz, and J. P. Wolf, *J. Chem. Phys.* **122**, 154103 (2005).  
<sup>63</sup>J. Lee, P. Pilch, S. Shoelson, and S. Scarlata, *Biochemistry* **36**, 2701 (1997).